

**Current Biology, Volume 24**

**Supplemental Information**

**EB1 Accelerates Two Conformational**

**Transitions Important**

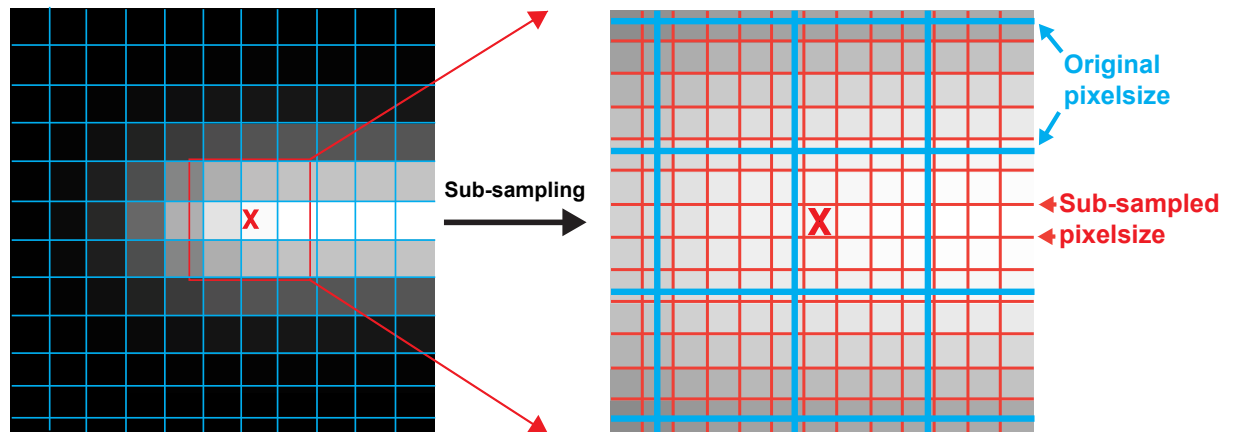
**for Microtubule Maturation and Dynamics**

**Sebastian P. Maurer, Nicholas I. Cade, Gergő Böhner, Nils Gustafsson,  
Emmanuel Boutant, and Thomas Surrey**

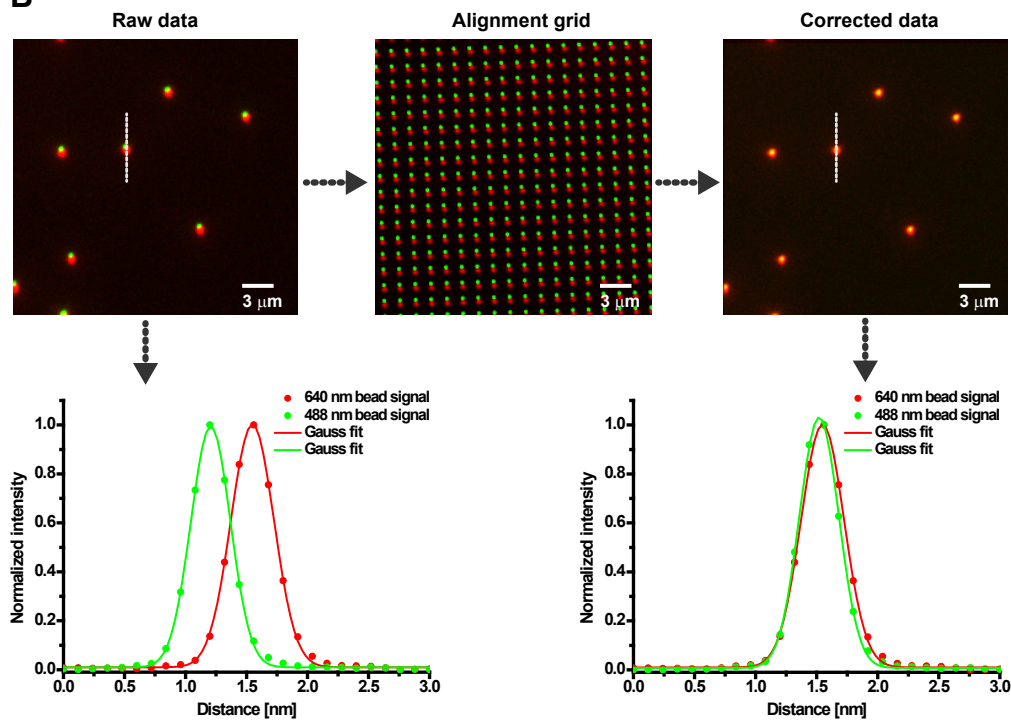
# Figure S1

**A**

**X** = microtubule end found by 2D-fitting during tracking



**B**



**C**

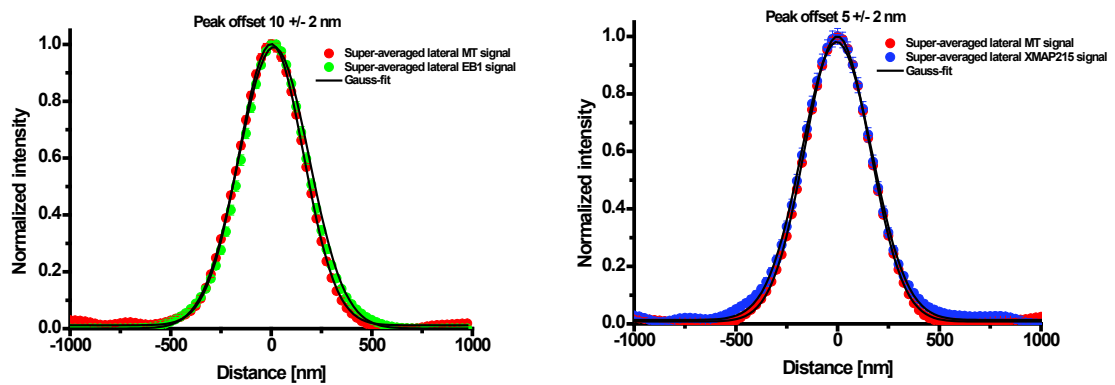


# Figure S2

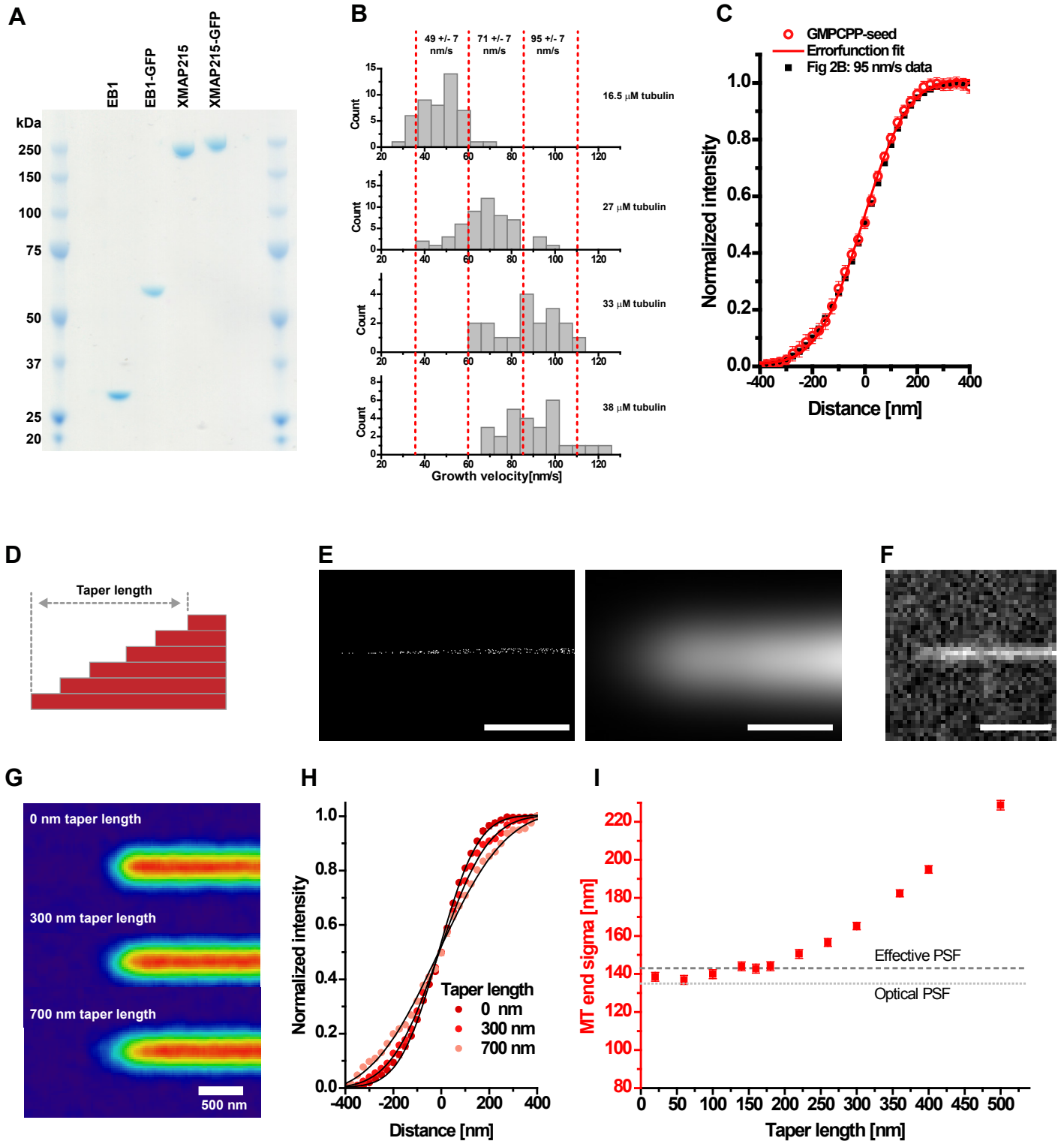


# Figure S3

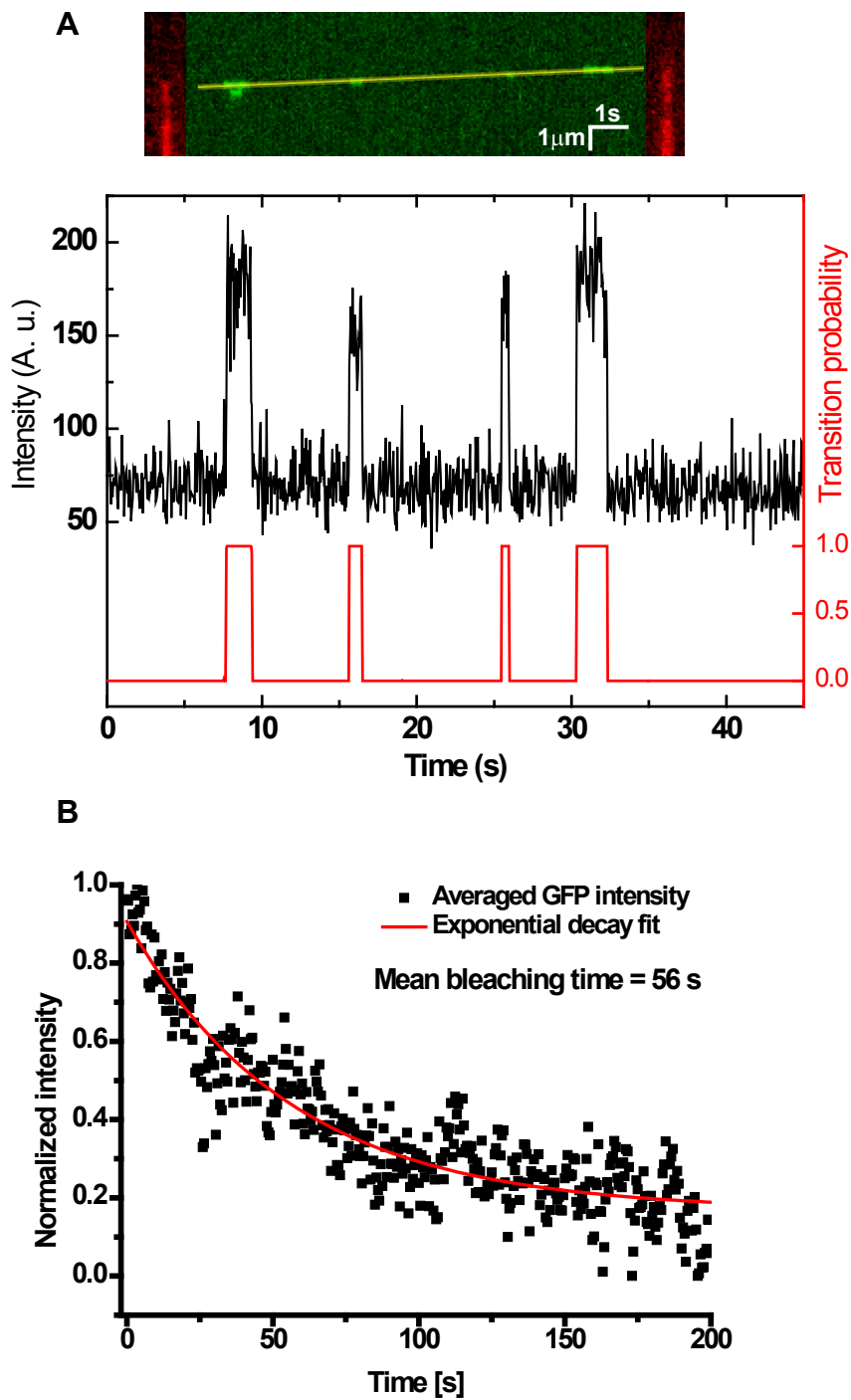


# Figure S4

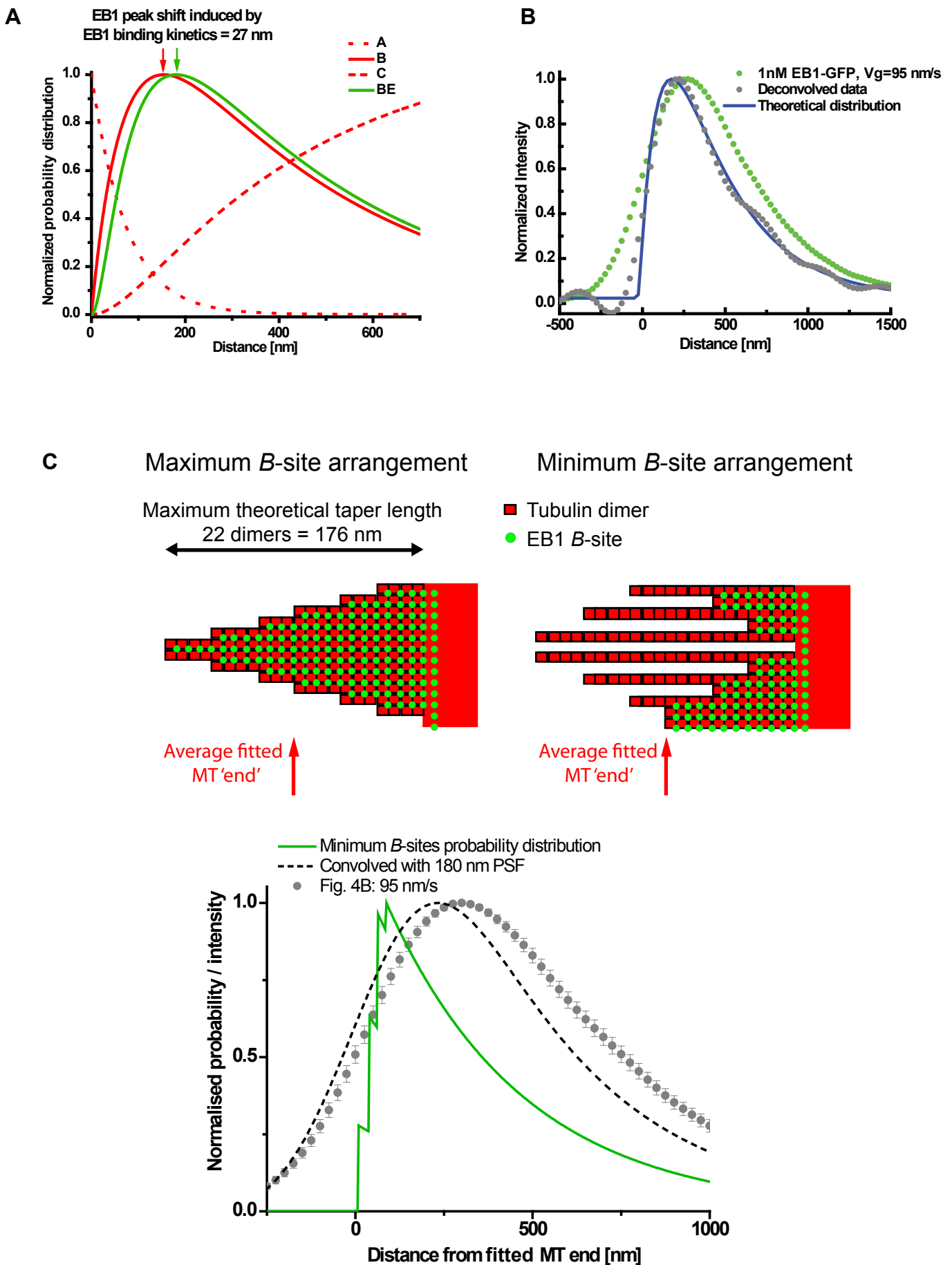


# Figure S5

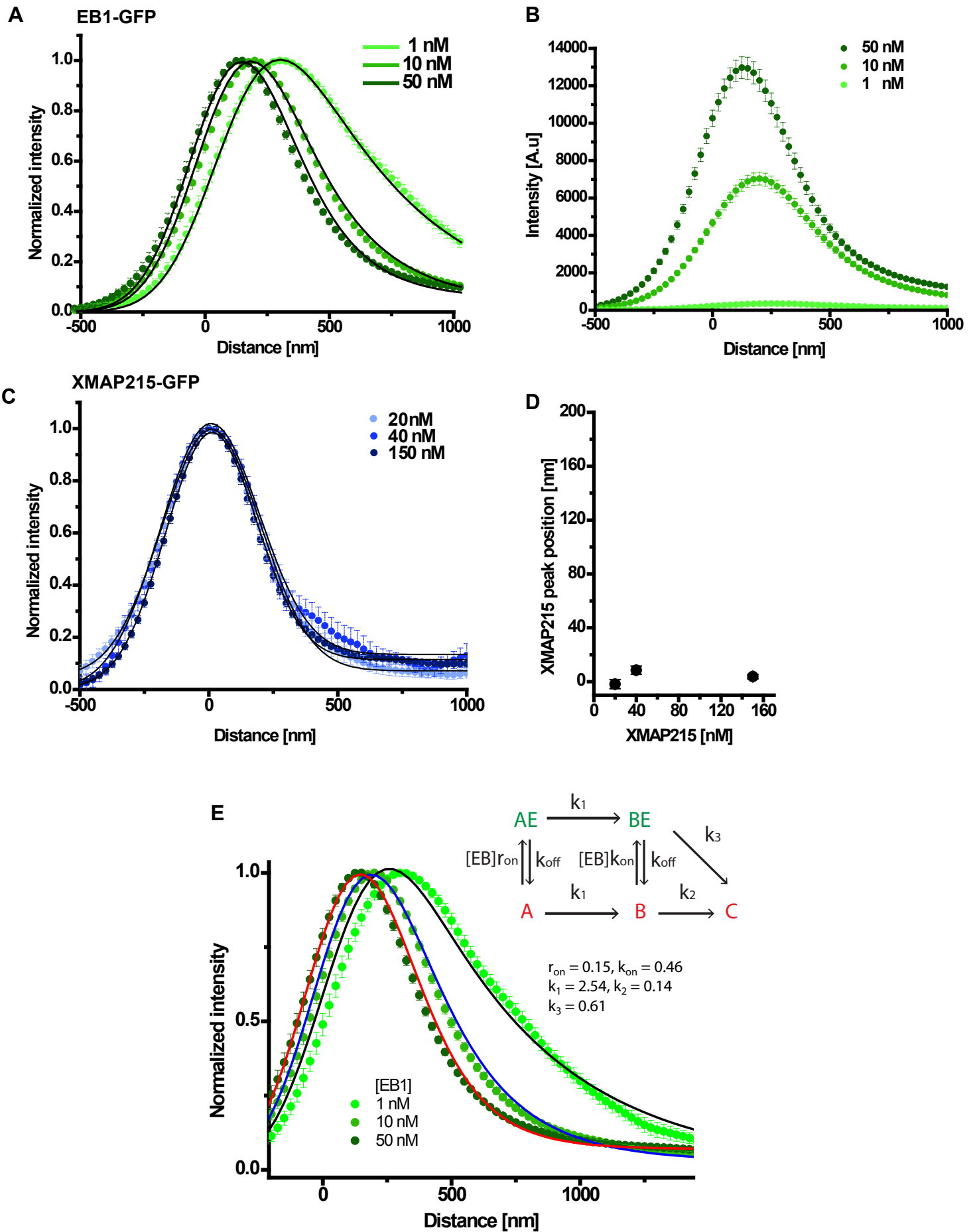


# Figure S6

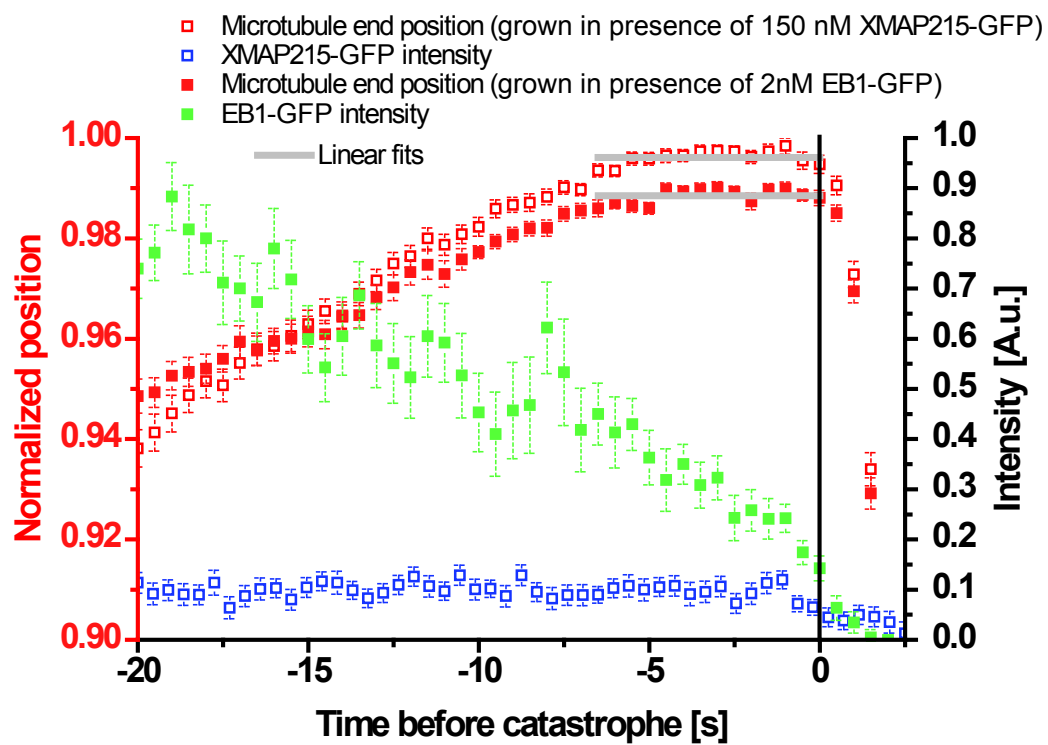
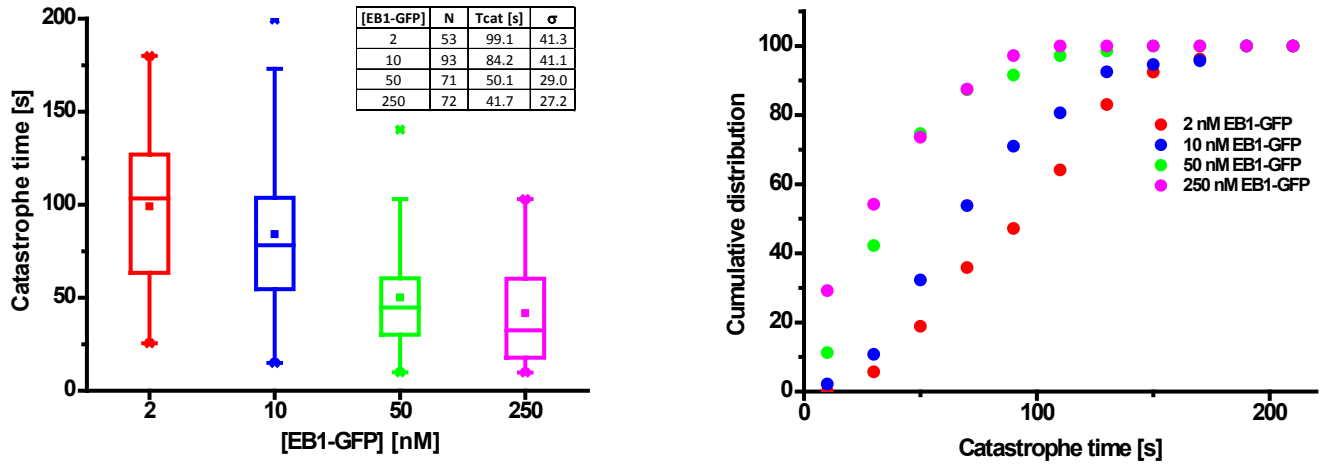


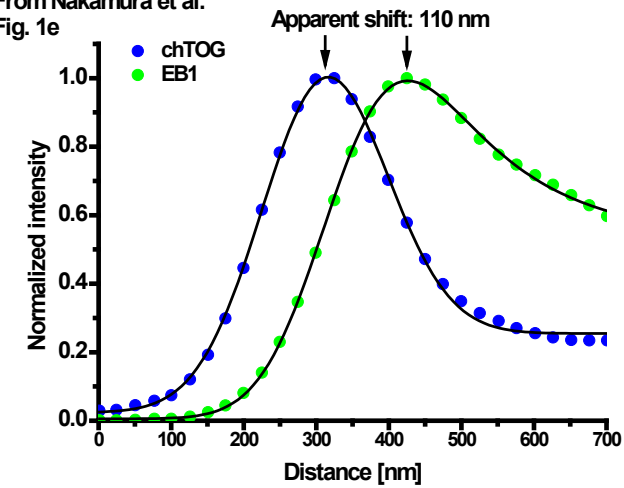
# Figure S7

**A**

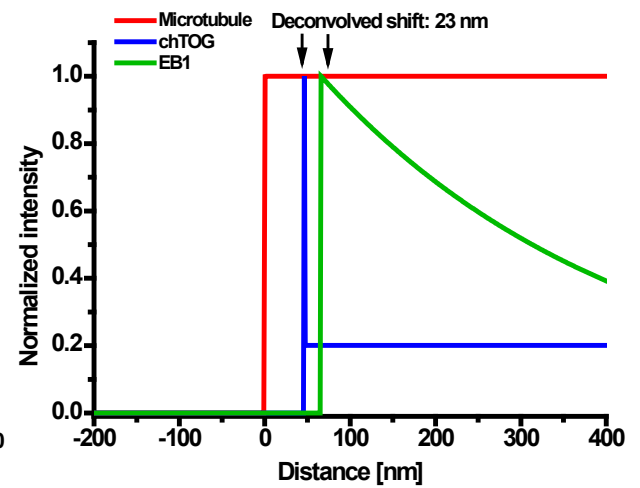
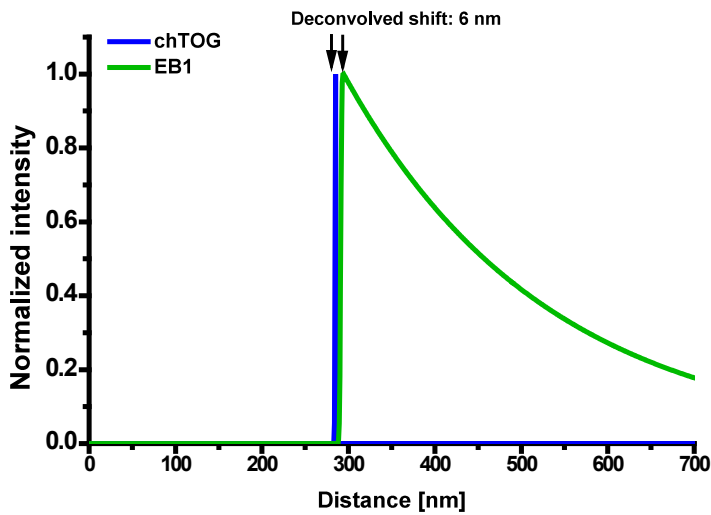
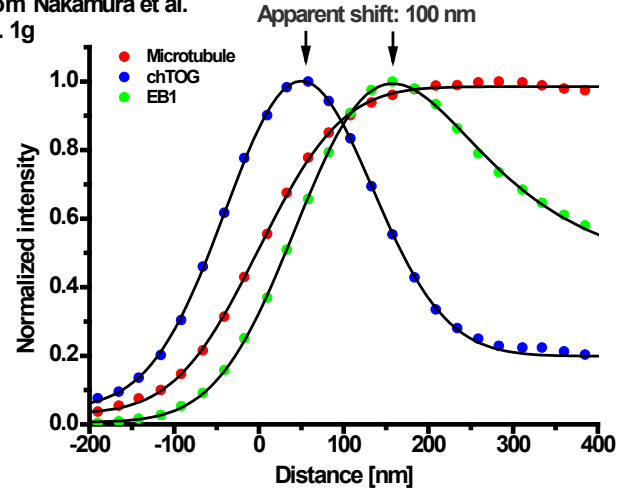


**B**

From Nakamura et al.  
Fig. 1e



From Nakamura et al.  
Fig. 1g





## SUPPLEMENTAL INFORMATION

### SUPPLEMENTAL FIGURE LEGENDS

**Figure S1. (A) Sub-pixel precision sub-sampling.** Left: Simulated image of a microtubule end. The microtubule end position which is found with sub-pixel size precision by a 2D-fit during the tracking procedure is marked by a red X. Right: Magnification of the area indicated by the box. The original image has been sub-divided into a new grid of 25 nm pixel size, centred around the X-position. The grey values of pixels have been recalculated based on a bicubic interpolation procedure. **(B) Precision of alignment of images recorded in different fluorescence channels.** Top: Overlay of TIRF microscopy images of 100 nm fluorescent beads recorded in the Cy5 and GFP channels (left, red and green, respectively); overlay of images of a calibration grid recorded in the two channels (middle), and the result of aligning the bead images using a transformation matrix obtained from the grid images (right). Bottom: One-dimensional intensity profiles (data points) and Gaussian fits (lines) for a bead measured in the Cy5 (red) and GFP (green) channel (along the white line in the bead images) before and after channel alignment. **(C) Precision of alignment after super-averaging.** Left panel: Lateral intensity profiles measured at the microtubule end position for Cy5-microtubules (red data points) and for associated EB1-GFP (green data points) with Gaussian fits (black line). The averaged curves are composed out of 48 growth episodes from different microtubules which corresponds to 5660 raw-images. Right panel: Lateral intensity profiles measured at the microtubule end position for Cy5-microtubules (red data) growing in the presence of XMAP215-GFP (blue data points). The averaged curves are composed of 94 growth episodes from different microtubules which corresponds to 8905 raw-images. All errors are standard error. All deviations of the position of the GFP-tagged microtubule end-tracking protein from the measured microtubule centre position are in the range of a few nanometres only, providing evidence for the close-to-molecular precision of position determination that our method provides.

**Figure S2. (A) Coomassie-stained SDS gels with the purified proteins used in this study. (B) Velocity sorting:** Histograms showing the distribution of microtubule growth velocities in experimental sets performed with four different tubulin concentrations, as indicated (1 nM EB1-GFP). The red dotted vertical lines indicate the 25 nm/s velocity ranges ( $\sim \pm 7$  nm/s standard deviation) used to sort and super-average data for defined velocity ranges (Fig. 2 and 4). This is in contrast to averaging all velocity data from experiments performed at the same tubulin concentration. **(C)** Super-averaged intensity profiles from 21 GMPCPP seeds (3117 images). The error function fit-derived PSF value was  $135 \pm 5$  nm. **(D-I) Simulations of the effect of tapering on microtubule end profiles** (D) Schematic of a taper formed by the linear increase in the extension of 6 protofilament ends. (E) A simulated microtubule end with 700 nm taper length before (left) and after (right) convolution with a Gaussian ( $\sigma = 135$  nm). The tubulin labelling ratio is 16 %. Scale bar is 400 nm. (F) As (E) after binning into 120 nm pixels and insertion into a typical experimental image. Scale bar is 2  $\mu$ m. (G) Super-averaged images of tracked simulated microtubules, with varying end taper

lengths, showing that large taper lengths are detected by our image analysis. (H) End profiles along the microtubule axis extracted from (G) with error-function fits. (I)  $\sigma$  value of error function fit from (H) as a function of simulated taper length. The dotted and dashed lines show the experimentally measured optical PSF and typical experimental effective PSF in our experiment. This curve shows that at our experimental SNR and for Cy5 labelling, end tapering is reliably detected above a length of  $\sim 180$  nm.

**Figure S3. (A) Single molecule measurements.** Top: Representative kymograph of a TIRF microscopy movie (50 ms exposure) showing single EB1-GFP binding events (green). The red frames on the left and right show the microtubule end position at the start and end of the kymograph. Tubulin concentration was 20  $\mu$ M, EB1-GFP concentration was 10 pM. Bottom: Left axis (black) – fluorescence intensity profile averaging over 2 pixels (80 nm per pixel) at the position of the microtubule end (yellow line in kymograph). Right axis (red) - transition probability profile of the raw intensity data from which dwell times and waiting times were measured (see Supplemental Methods). **(B) Bleaching time analysis.** Mean GFP fluorescence intensity (black data points) integrated over the entire field of view of a TIRF microscopy movie of Cy5-microtubules growing in the presence of 1 nM EB1-GFP and 27  $\mu$ M tubulin. Exposure times and rates were the same as used for dual-colour recording of dynamic microtubules. A mono-exponential decay fit to the data gives a mean bleaching time of 56 s, i.e. approximately an order of magnitude larger than the lifetimes of the conformational states at the microtubule end region.

**Figure S4. (A) Theoretical molecular distributions** of the different microtubule maturation states *A*, *B*, and *C*, (red) and of bound EB1-GFP (green), calculated using the parameter values of the fit to the 95 nm/s EB1-GFP profile in Fig. 4. This figure shows that the peak of the molecular EB1-GFP profile (BE state) is slightly shifted with respect to the peak of the EB1 binding sites, *B* (by 27 nm or  $\sim 3$  tubulin lengths at the highest growth velocity studied here). **(B) Direct intensity profile deconvolution.** Super-averaged fluorescence intensity profile of EB1-GFP (green data points) as shown for 95 nm/s in Fig. 4B, and the underlying molecular EB1-GFP distribution (blue line) from Fig. 4C. The grey dotted line shows the result of directly deconvolving the fluorescence intensity profile with a Gaussian representing the measured effective PSF. This result shows that a direct deconvolution of the data produces a similar molecular density distribution as our method of extracting the distribution from a fit using a convolved model. However, due to experimental noise and a limited data range, the numerical deconvolution produces a less accurate profile. **(C) Tapering alone does not explain the measured EB1 shift.** Top: The average taper length in our experiments is between 0 and  $\sim 180$  nm (Fig. S2D-I). Here we show schematics for the maximum theoretical taper length of 176 nm, as measured from end to end (22 dimers – red squares). The microtubule has been unrolled to show 13 protofilaments. EB1 binding sites are assumed to form at the junction of four dimers. After convolution with an optical PSF, the fitted ‘end’ of the Cy5-microtubule will correspond to a position halfway along the taper. In a model without the first transformational step *A*  $\rightarrow$  *B*, EB1 binding sites are assumed to decay exponentially along the taper for each viable protofilament junction. Two extreme examples for different tapering geometries are shown using the

same protofilament lengths (hence giving the same fitted microtubule end position), to maximise (left) and minimise (right) the number of  $B$  sites in the taper. Bottom: The resulting average  $B$  site probability for the minimum  $B$  site geometry (green line) and the result of convolution with a 180 nm PSF (black dashed line). This shows that even if the protofilaments adopt a highly filamented end structure (right configuration, rather unlikely), the resultant offset between the microtubule end position and EB1 peak would only partly explain the large shift observed at high growth velocity (Fig. 4B). Binding kinetics would only create a small additional shift (Fig 3D, Fig S4A). For shorter taper lengths and more realistic tapering geometries, the observed shifts of the EB1 binding sites are even less likely to be explained by tapering alone. Error bars are SE.

**Figure S5. (A) Two-step model with binding kinetics fitted to EB1-GFP intensity profiles for different EB1-GFP concentrations.** Data as in Fig. 5B. The black lines are fits with our two-step model with binding kinetics with free (unshared) rate constant parameters. Parameter values derived from this fit are shown in Table S1. **(B) Intensity profiles shown in A before normalization.** **(C-D) Effect of XMAP215 concentration on its end position.** (C) Super-averaged XMAP215-GFP fluorescence intensity profiles for microtubules growing in the presence of 20, 40 and 150 nM XMAP215-GFP. The tubulin concentrations were 24, 21, 11.3  $\mu\text{M}$ , respectively. The super-averaged profiles were generated from 997 to 8905 images in total. The black lines show individual fits to the three intensity profiles using the Gauss-Lattice model. (D) The molecular peak positions of XMAP215-GFP as determined from the fits to the intensity profiles in B. (E) Super-averaged data as in Fig. 5B. The solid lines show a global fit to the data sets assuming low affinity EB1 binding to the initial  $A$  state of the microtubule, with an associated on-rate of  $r_{\text{on}}$  (where  $r_{\text{on}} < k_{\text{on}}$  for the  $B$  state). Inset: Modified kinetic model (cf. Fig. 5A). The rate constants  $k_{1-3}$ ,  $k_{\text{on}}$ ,  $r_{\text{on}}$  are shared fitting parameters for all three concentrations. In this model EB1 has no effect on the first maturation rate constant  $k_1$ . The model produces a significantly worse global fit to the data than the three state model with varying  $k_1$ . In particular the data at the lowest EB1 concentration cannot be explained satisfactorily by this model. Error bars are SE.

**Figure S6. Comparison of EB1 and XMAP215 behaviour before catastrophe.** (Left axis) Averaged microtubule end position as a function of time prior to catastrophe for microtubules growing in the presence of 2 nM EB1-GFP and 20  $\mu\text{M}$  tubulin or 150 nM XMAP215-GFP and 11.3  $\mu\text{M}$  tubulin. (Right axis) The corresponding fluorescence intensity before catastrophe for EB1-GFP and XMAP-GFP, as indicated. The grey lines indicate the duration of the growth pauses before catastrophe (Suppl. Experimental Procedures) Error bars are SE.

**Figure S7. Fluorescence intensity profiles extracted from structured illumination microscopy images of microtubule ends in fixed cultured cells as reported in [S 1].** (A) Box plots (left) and cumulative distributions (right) of catastrophe times at different EB1-GFP concentrations and constant tubulin concentration (20  $\mu\text{M}$ ) for the data shown in Fig. 7B and D. Catastrophe times are the inverse of the catastrophe frequencies. (B) Top: Extracted data from Fig. 2d and Fig. 1g of Ref. [S 1], with fits using the models used in Fig. 2 of this study. Bottom: The extracted molecular distributions as obtained from the fits to the above data. A comparison of the fluorescence intensity profiles and the

molecular density distributions illustrates that the distance between the apparent peak positions of the EB1 and XMAP215 fluorescence intensity profiles differs by up to 100 nm from the difference of the peak position of the underlying molecular density distributions. This is a consequence of the convolution of the density distributions with the PSF. These discrepancies exist although the PSF is smaller in structured illumination microscopy than in conventional TIRF microscopy, as confirmed by the fits to the published data ( $\sigma$  values obtained from the fits were 70-90 nm).

## SUPPLEMENTAL TABLES

**Table S1 – Fitting parameters**

Figure	Growth velocity [nm/s]	EB1 conc. [nM]	k <sub>1</sub> [s <sup>-1</sup> ]	k <sub>2</sub> [s <sup>-1</sup> ]	k <sub>3</sub> [s <sup>-1</sup> ]	a <sub>1</sub> [Arb. u.]	a <sub>lat</sub> [Arb. u.]	σ [nm]	χ <sup>2</sup>
4B	49	1	1.39 ± 0.05 <sup>†</sup>	0.24 ± 0.003 <sup>†</sup>	0	1.9 ± 0.09	0.02 ± 0.0 <sup>†</sup>	185 ± 0.9 <sup>†</sup>	1.7
	71	1				1.56 ± 0.07			
	95	1				1.37 ± 0.07			
S5	95	1	1.14 ± 0.06	0.23 ± 0.004	0	0.72 ± 0.04	0.02 ± 0.0	183 ± 1 <sup>†</sup>	5.4
	98	10	6.5 ± 0.8	0.55 ± 0.01		29 ± 46	0.04 ± 0.0		
	93	50	10	0.60 ± 0.01		2.79 ± 0.03	0.07 ± 0.0		
5B	95	1	1.14	0.23 ± 0.01 <sup>†</sup>	0.73 ± 0.01 <sup>†</sup>	0.83 ± 0.02	0.02	183 <sup>†</sup>	5.75
	98	10	6.5			13.9 ± 0.2	0.04		
	93	50	10			26.3 ± 0.3	0.07		
Values without errors are fixed fitting parameters. Other fixed parameters for all fits: k <sub>on</sub> (0.15 s <sup>-1</sup> nM <sup>-1</sup> ), k <sub>off</sub> (3.4 s <sup>-1</sup> ) †Globally shared free parameters.									

**Table S1. Fitting parameters obtained from fitting the two-step maturation model with binding kinetics to the data in the figures shown.**

**Table S2 – Estimation of errors**

Error	Cy5 Microtubule channel	GFP channel	Note
<b>Optical PSF <math>\sigma</math></b>	135 nm	115 nm	The optical PSF of the microscope obtained from 200 nm diameter beads
<b>Effective PSF</b>			A combination of the optical PSF, and broadening due to the alignment and averaging procedures
Axial, $\sigma_{ax}$	143 nm	180 nm	
Lateral, $\sigma_{lat}$	158 nm	169 nm	
<b>Position precision</b>			†Determined by tracking simulated microtubules (Fig. S2D-I) with a 20nm taper and corresponding ‘GFP’ point-like signal. *Estimated from Fig. S1C.
Axial, $\delta x_{ax}$	4 nm†	8 nm†	
Lateral, $\delta x_{lat}$	2 nm†	16 nm*	

**Table S2. An estimation of the final errors in effective PSF width and position precision.** Cy5-microtubule intensity profiles and their corresponding XMAP215-GFP profiles along the microtubule axis were fitted with error-functions and Gaussian functions, respectively; lateral profiles perpendicular to the microtubule axis were fitted with Gaussian functions: the fit  $\sigma$  values and end positions were obtained. A bootstrapping approach was used to generate a distribution of  $\sigma$  values of fits to super-averages of different groups of intensity profiles. The mean of the resulting distribution provides an estimate for the  $\sigma$  value of the effective PSF. The position precision was estimated by tracking simulated microtubules and associated point-like GFP signal. The tracked position values were compared to the original simulated coordinates.

## SUPPLEMENTAL EXPERIMENTAL PROCEDURES

### Experiments:

**Protein biochemistry:** Full-length human EB1 [GeneBank accession number GQ129296] was cloned into the pETMz2 bacterial expression vector, generating a construct coding for human EB1 with an N-terminal hexahistidine-Z-tag followed by a TEV protease cleavage site and with EGFP fused to the EB1 C-terminus via a hexaglycine linker. For the generation of an EB1 construct without GFP, a stop codon was inserted at the 3'-end of the EB1 coding sequence. EB1-GFP and EB1 were expressed in E.coli and purified (IMAC, TEV cleavage, gel filtration) as described for the fission yeast homolog Mal3 [S 2]. *Xenopus laevis* XMAP215 and XMAP215-GFP [S 3] with C-terminal heptahistidine tags were expressed in insect cells and purified similar to described procedures (IMAC, gel filtration) [S 4], however using the same columns and buffers as for EB1. All proteins were kept in storage buffer (50 mM NaPi pH 7, 400 mM KCl, 2 mM MgCl<sub>2</sub>, 0.8 mM  $\beta$ -mercaptoethanol, 1% glycerol, 0.005% Brij-35). Porcine brain tubulin was prepared and labelled as described previously [S 5, 6].

**TIRF microscopy:** The in vitro reconstitution of microtubule end tracking was realised as described previously [S 7]. Final protein concentrations were 20-150 nM XMAP215-GFP, 1-50 nM EB1-GFP, 11.3-38  $\mu$ M tubulin (containing 9% Cy5-labelled tubulin). The final buffer consisted of 72% assay buffer (80 mM K-PIPES pH 6.8, 85 mM KCl, 14 mM MgCl<sub>2</sub>, 10 mM  $\beta$ -mercaptoethanol, 0.005 % Brij-35), supplemented with 20 mM glucose, 320  $\mu$ g/ $\mu$ l glucose oxidase, 55  $\mu$ g/ $\mu$ l catalase, 0.12 % methylcellulose 4000, 1 mM GTP), 20% BRB80 (80 mM PIPES pH 6.8, 1 mM MgCl<sub>2</sub>, 1 mM EGTA) and 8% storage buffer. The temperature was 30°C. For simultaneous dual-colour time-lapse imaging of the Cy5 and GFP channel, images with 300 ms exposure time were simultaneously recorded every 0.5 s onto two Evolve 512 (Photometrics, UK) EMCCD cameras mounted on an iMIC (TILL Photonics, Germany) total internal reflection fluorescence (TIRF) microscope (1.33x additional optical magnification). This was equipped with 488 nm and 640 nm diode lasers (Toptica, Germany), 100x 1.49 N.A (Olympus, Japan) objective lens, a quadband dichroic mirror (405/488/561/64, Semrock, USA), and GFP (525/50, Semrock, USA) and Cy5 (700/75, Semrock, USA) emission filters. For spatial channel registration, images of a calibration grid with 500 nm features (Compugraphics, UK) were recorded simultaneously in the Cy5 and GFP channels using transmitted bright-field illumination. For controls, images with 100 nm TetraSpeck (Invitrogen, UK) fluorescent beads were recorded simultaneously in the Cy5 and GFP channels.

**Single molecule measurements:** Single molecule EB1-GFP binding to growing Cy5 microtubule ends were recorded with TIRF microscopy (150x objective lens, 50 ms exposure (streaming acquisition), 20  $\mu$ M tubulin, 10 pM EB1-GFP). Kymographs were created for each microtubule, over 500 s (Fig. S3A). An emission intensity trace was produced by averaging over 2 pixels (80 nm per pixel) at the position of the microtubule end for the entire movie. The emission traces from 60 kymographs were combined and analysed using a single molecule analysis program [S 8] to produce a transition probability trace (Fig. S3A lower trace). A MATLAB script was used to extract histograms of the dwell times of each transition (Fig. 3B top) and the waiting times between successive

transitions (Fig. 3B bottom). The distributions are well fit with exponential decays, as expected for stochastic Poisson unbinding and binding processes, giving the characteristic transition rates  $k_{\text{off}}$  and  $k_{\text{on}}$ , respectively. The association rate constant per binding site was estimated by assuming 100 binding sites within the 160 nm line-width (as calculated from the probability distribution for the lowest EB1 concentration in Fig. 5C).

**EB1 binding curve:** The EB1 binding curve was measured by TIRF microscopy as described previously [S 2]. Briefly: Microtubules (20  $\mu\text{M}$  tubulin) were grown in the presence of 0.125 to 300 nM EB1-GFP. At least 10 microtubules from different parts of the field of view were tracked and super-averaged EB1-GFP fluorescence profiles were created as described below (from at least 1451 images). The maximal intensity values of the resulting intensity profiles were then plotted against the EB1 concentration and fitted with a one-site binding model to obtain the dissociation constant  $K_D$ .

### **Data Analysis:**

**Automated microtubule end tracking:** Microtubule ends recorded in the Cy5 channel were automatically tracked by a MATLAB program (MathWorks, USA). This uses elements of the FIESTA microtubule tracking program [S 9], which was originally developed for microtubule gliding experiments. Here, we introduced modifications to improve the tracking reliability for microtubules growing in the presence of substantial concentrations of fluorescently labelled soluble tubulin. Improvements were achieved using an additional Wiener filter and also a highly configurable Wallis filter on the images; the latter eliminated problems arising from inhomogeneous fluorescence excitation and made intensity signals from different parts of the field of view more comparable. Other modifications include the creation of binary images from filtered images using information from earlier-time-frame images, such as the previous microtubule end position and orientation, and using statistics on the microtubule growth velocity, and the frequency and length of shrinkage periods. This is a substantial change to the FIESTA control flow, as we treat frames explicitly as a time series during tracking. Using FIESTA functionalities, areas belonging to individual microtubules were identified in these binary images. Two-dimensional models were then fitted to areas in the original (unfiltered) images where microtubules had been identified, describing the microtubules as a Gaussian wall and their ends as a half-Gaussian. The maximum of the half-Gaussian end function was determined with sub-pixel precision and used as a reference point for image alignment before averaging.

**Time-averaging of images around a growing microtubule end with sub-pixel precision:** For individual microtubule growth episodes, images of 6.4  $\mu\text{m}$  x 6.4  $\mu\text{m}$  size (in sample space) were cropped from the original (unfiltered) Cy5-microtubule images of a time-lapse movie. The positioning of the cropped images around the detected microtubule end position was performed with sub-pixel precision. This was achieved by cubic interpolation of the original 120 x 120 nm image pixels, into a grid of 25 x 25 nm pixels placed such that the detected microtubule end was in the exact centre of the image (Fig. S1). The denser grid allowed more precise alignment during subsequent averaging. The



cropped images belonging to one growth episode of a microtubule (typically 80 - 200 images) were then averaged, generating a time-averaged image.

**Time-averaging of images with EB1-GFP and XMAP215-GFP with sub-pixel precision:** Time averaging EB1-GFP or XMAP215-GFP images correctly relative to the microtubule end position required exact knowledge of registration between the two cameras used to simultaneously record the images in the Cy5 and GFP channels. At each specific position in the image corresponding to the microtubule end, the local degree of misalignment was determined from images of a calibration grid [S 10]. This correction was applied for each microtubule end position before cropping corresponding images in the GFP channel. Averaging was done as for the Cy5 channel. This procedure generated time-averaged EB1-GFP or XMAP215-GFP images with spatial coordinates identical to those of the corresponding time-averaged microtubule images.

**Super-averaging of time-averaged profiles:** After time-averaging an individual microtubule growth episode, we extracted one-dimensional intensity profiles along the microtubule axis (axial profiles), for both microtubule and end binding protein channels. The microtubule end position for each axial profile was determined by assuming an underlying step function for the molecular tubulin distribution, convolved with a Gaussian representing the effective point spread function (PSF) of the optical system and the effects of averaging (Fig. 1B). This gives an error function of the form

$$MT(x) = a_0 \left[ 1 + \operatorname{erf}\left(\frac{z_{mt}}{\sqrt{2}}\right) \right]$$

where  $a_0$  is a constant, erf is the error function,  $z_{mt} = (x - x_c)/\sigma$ ,  $x_c$  is the microtubule end position, and  $\sigma$  is a measure of the width of the convolving Gaussian ( $\sigma$  is  $\sim 0.42$  times the full width of the Gaussian at half maximum, Fig. 1B). This fitting allowed the alignment with respect to the microtubule end position and ‘super-averaging’ of different time-averaged microtubule profiles and their associated EB1-GFP or XMAP215-GFP profiles, from microtubules growing in different positions and orientations at different times in different movies. This super-averaging (typically 20 to 100 time-averaged profiles) resulted in a total of typically 1000 to 10000 individual image frames to be included in the super-averages.

For control purposes, we also generated one-dimensional profiles perpendicular to the microtubule axis at the position of the growing microtubule end (lateral profiles). A simple Gaussian was fitted to these profiles to determine the centre position with respect to which super-averaging of lateral profiles was performed (Fig. S1C). The final lateral alignment precision reached after super-averaging was 16 nm or smaller.

To measure the axial PSF on effectively blunt microtubules for control purposes, GMPCPP seeds were diluted in assay buffer containing 1 mM GMPCPP instead of GTP and no free tubulin. After 30 minutes, seeds were imaged with the same imaging settings as for experiments with growing microtubules. 21 seed ends were tracked, time-averaged and subsequently super-averaged to generate an intensity profile combining information from 3117 images. The profile was fitted with the error function model to obtain the PSF value.

**Velocity-sorting of intensity profiles from time-averaged images:** Microtubule growth velocities at a certain tubulin concentration vary around a mean value. As the fluorescence intensity signal of EB1-GFP depends on the microtubule growth velocity, we aimed to reduce the deviation of microtubule growth velocities within one set of intensity profiles from time-averaged images used to create a super-average. In order to do so, intensity profiles obtained from time-averages from different experiments were re-binned to select growth velocities with smaller growth variation as shown for 1 nM EB1-GFP data in Fig. S2B, and were subsequently super-averaged. Data in Fig. 6A, B were not velocity-sorted, because due to the growth promoting effect of XMAP215, there was not sufficient overlap between velocity distributions between experiments with and without XMAP215, even with adjusted tubulin concentrations.

**Extracting molecular distributions from super-averaged axial fluorescence intensity profiles:**

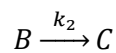
The physical microtubule end position was obtained from a fit to super-averaged fluorescence intensity profiles as described in the previous paragraph. To fit super-averaged XMAP215-GFP fluorescence intensity profiles, the underlying molecular distribution was modelled as a delta function (representing microtubule end accumulation) with an additional step function (to account for weak binding to the mature microtubule lattice) (Fig. 2K). This function was convolved with a Gaussian representing the PSF of the optical system and the effects of averaging, giving

$$XMAP(x) = a_1 e^{-\frac{1}{2}z_X^2} + a_{lat} \left[ 1 + \operatorname{erf}\left(\frac{z_X}{\sqrt{2}}\right) \right]$$

where  $z_X = \frac{x-x_c}{\sigma}$ , and  $a_{lat}$  is the intensity of weak lattice binding (Gauss-Lattice model).

To fit super-averaged EB1-GFP fluorescence intensity profiles we tested a range of different models for the underlying molecular distributions, as discussed in the main text. All models assumed a specific kinetic scenario for the appearance and disappearance of EB1 binding sites in the microtubule end region. The microtubules analysed here were tracked only during phases of continuous and uniform growth; hence, assuming steady state these kinetic events are assumed to be directly represented by the spatial distributions of the bound molecules as measured with respect to the growing microtubule end. For fitting the fluorescence intensity distributions, all models below were convolved with a Gaussian (width  $\sigma$ ) to account for the optical PSF and effects of averaging, and fitting parameters were iteratively varied.

The simplest model was based on assuming instantaneous formation of EB1 binding sites "B" with bound EB and their transformation in a single step with a rate constant  $k_2$  into weak binding sites "C" in older parts of the microtubule:



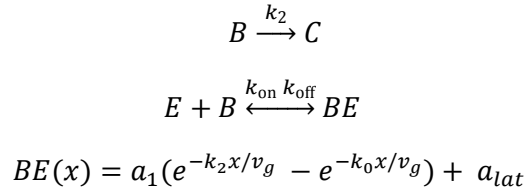
Both the time course and the equivalent spatial profile of "B" at a growing microtubule end are mono-exponential decays (Fig. 2E):

$$B(x) = a_0 e^{-\frac{k_2(x-x_c)}{v_g}}$$

where the microtubule growth velocity is  $v_g = x/t$ , and  $x_c$  accounts for any spatial offset from the microtubule end position. This function was then convolved with a Gaussian during fitting of the super-averaged EB1-GFP intensity profiles (exponentially modified Gaussian model).

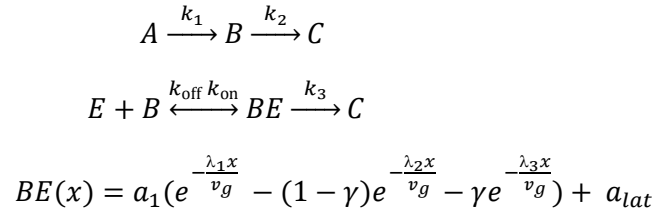
The following schemes summarise other models used for the molecular distributions, where  $E$  = free EB1 (assumed to be a constant concentration),  $B$  = EB1 binding site,  $BE$  = bound EB1,  $C$  = mature EB1 non-binding state:

One-step model with binding kinetics (Fig. 3A):



where  $k_0$  is found by solving the relevant rate equations and depends on  $E$ ,  $k_{\text{on}}$ ,  $k_{\text{off}}$ ,  $k_2$ .  $a_{\text{lat}}$  is a step function representing a constant background signal due to lattice binding

Two-step model with binding kinetics (Fig. 5A):



where  $\lambda_i$ ,  $\gamma$  are found by solving rate equations.

We tested a version of this two-step model with additional low affinity EB1 binding to the  $A$  state, and no variation in the first maturation time  $k_1$  (Fig. S5E). This was *not* able to account for the peak shifts seen in Fig. 5B where EB1 concentrations were varied.

Manual data analysis, fitting, and graphing was performed with Origin 8.5 software (OriginLab, USA). The range used to fit super-averaged intensity profiles was set to -1,000 nm to +2,000 nm for EB1-GFP and XMAP215-GFP profiles and to - 400 nm to + 400 nm for Cy5-microtubule end profiles. Weighted fits were performed to super-averaged intensity profiles using the standard error of the individual averaged data points.

The total maturation time of the microtubule end was defined as the sum of  $k_1^{-1} + k_{\text{BC}}^{-1}$ , where  $k_{\text{BC}} = (1-\theta)k_2 + \theta k_3$  and  $\theta$  is the fractional EB1 occupancy of the  $B$  sites.

**Estimation of errors:** An estimation of the errors introduced at different stages of the profile fitting analysis is summarized in Table S2.

**Catastrophe event alignment and analysis:** During the automated tracking procedure described above, the microtubule end position and corresponding total EB1-GFP intensity in the end region were simultaneously recorded. A MATLAB algorithm was used to identify catastrophe events based on a rapid reduction in microtubule length, generating a position-time profile around a catastrophe event [S 11]. For each specific growth condition (EB1 / tubulin concentration), all such detected individual microtubule catastrophe profiles were temporally aligned using an iterative procedure and averaged using a MATLAB routine based on a modified Excel macro [S 12]. For each averaged catastrophe position-time profile, the corresponding aligned and averaged total EB1 intensity-time profile was generated and fitted with an empirical exponential-decay function. Pause times were defined by fitting a zero gradient line to the microtubule end position data points and restricting the fit range to give  $\chi^2 < 1.5$ .

**Catastrophe time determination:** Catastrophe times were determined from the same TIRF microscopy data also used for catastrophe event alignment and growth pause analysis. The duration of microtubule growth from the first visually detectable extension of the GMPCPP seed until the time point of catastrophe was manually measured on kymographs by using the straight line selection tool of ImageJ.

**End tapering simulations:** Images of dynamic microtubule growth were simulated in MATLAB similar to previously described simulations [S 13]; in addition random orientations, fluctuations in the growth rate, and fluctuating lateral displacements of the end were included. The microtubule structures were convolved with a Gaussian ( $\sigma = 135$  nm from our experimentally determined optical PSF, Table S2), and then binned into 120 nm pixels (corresponding to the pixel size of our experimental images). The simulated microtubules were intensity matched to experimental levels and inserted into an unobstructed region of a real experimental image series to generate simulated microtubules in the presence of experimental noise. The microtubules were then tracked and analysed as described above to determine the effect of differently long microtubule end tapers on the tracking accuracy and the detected effective PSF (Fig. S2I).

## SUPPLEMENTAL REFERENCES

- S 1. Nakamura, S., Grigoriev, I., Nogi, T., Hamaji, T., Cassimeris, L., and Mimori-Kiyosue, Y. (2012). Dissecting the nanoscale distributions and functions of microtubule-end-binding proteins EB1 and ch-TOG in interphase HeLa cells. *PLoS One* 7, e51442.
- S 2. Maurer, S.P., Bieling, P., Cope, J., Hoenger, A., and Surrey, T. (2011). GTPgammaS microtubules mimic the growing microtubule end structure recognized by end-binding proteins (EBs). *Proc Natl Acad Sci U S A* 108, 3988-3993.
- S 3. Widlund, P.O., Stear, J.H., Pozniakovsky, A., Zanic, M., Reber, S., Brouhard, G.J., Hyman, A.A., and Howard, J. (2011). XMAP215 polymerase activity is built by combining multiple tubulin-binding TOG domains and a basic lattice-binding region. *Proc Natl Acad Sci U S A* 108, 2741-2746.
- S 4. Brouhard, G.J., Stear, J.H., Noetzel, T.L., Al-Bassam, J., Kinoshita, K., Harrison, S.C., Howard, J., and Hyman, A.A. (2008). XMAP215 is a processive microtubule polymerase. *Cell* 132, 79-88.
- S 5. Castoldi, M., and Popov, A.V. (2003). Purification of brain tubulin through two cycles of polymerization-depolymerization in a high-molarity buffer. *Protein expression and purification* 32, 83-88.
- S 6. Hyman, A., Drechsel, D., Kellogg, D., Salser, S., Sawin, K., Steffen, P., Wordeman, L., and Mitchison, T. (1991). Preparation of modified tubulins. *Methods Enzymol* 196, 478-485.
- S 7. Bieling, P., Telley, I.A., Hentrich, C., Piehler, J., and Surrey, T. (2010). Fluorescence microscopy assays on chemically functionalized surfaces for quantitative imaging of microtubule, motor, and +TIP dynamics. *Methods Cell Biol* 95, 555-580.
- S 8. Greenfeld, M., Pavlichin, D.S., Mabuchi, H., and Herschlag, D. (2012). Single Molecule Analysis Research Tool (SMART): an integrated approach for analyzing single molecule data. *PLoS One* 7, e30024.
- S 9. Ruhnnow, F., Zwicker, D., and Diez, S. (2011). Tracking single particles and elongated filaments with nanometer precision. *Biophys J* 100, 2820-2828.
- S 10. Evangelidis, G.D., and Psarakis, E.Z. (2008). Parametric image alignment using enhanced correlation coefficient maximization. *IEEE transactions on pattern analysis and machine intelligence* 30, 1858-1865.
- S 11. Maurer, S.P., Fourniol, F.J., Bohner, G., Moores, C.A., and Surrey, T. (2012). EBs recognize a nucleotide-dependent structural cap at growing microtubule ends. *Cell* 149, 371-382.
- S 12. Katsuki, M., Drummond, D.R., Osei, M., and Cross, R.A. (2009). Mal3 masks catastrophe events in *Schizosaccharomyces pombe* microtubules by inhibiting shrinkage and promoting rescue. *J Biol Chem* 284, 29246-29250.
- S 13. Demchouk, A.O., Gardner, M.K., and Odde, D.J. (2011). Microtubule Tip Tracking and Tip Structures at the Nanometer Scale Using Digital Fluorescence Microscopy. *Cellular and molecular bioengineering* 4, 192-204.